

A Deep Learning Framework: Predicting Fire Radiative Power From the Combination of Polar-Orbiting and Geostationary Satellite Data During Wildfire Spread

Xixun Dong , Change Zheng , Fengjun Zhao , Guangyu Wang , Ye Tian , and Hongchen Li 

Abstract—Fire radiative power (FRP) is a key indicator for evaluating the intensity of wildfires, unlike traditional real-time fire lines or combustion areas that only provide binary information, and its accurate prediction is more important for firefighting actions and environmental pollution assessment. To this end, we used a combination of data from geostationary satellites and polar orbit satellites to correct the FRP data. Incorporating various factors that affect wildfire spread, such as meteorological conditions, topography, vegetation indexes, and population density, we constructed a comprehensive California wildfire spread dataset, covering information since 2017. Then, we established a deep learning framework that integrates various modules to analyze multimodal data for the accurate prediction of FRP imagery. We investigated the impact of input sequence length and loss function design on model predictive performance, leading to subsequent model optimization. Furthermore, our model has demonstrated acceptable performance in transfer learning and multistep prediction, emphasizing its application value in wildfire prediction and management. It can provide more detailed information about wildfire spread, showcasing the powerful capability of deep learning to process multimodal data and its potential in the emerging field of real-time FRP prediction.

Index Terms—Deep learning, fire radiative power (FRP), remote sensing, spatiotemporal prediction, wildfire.

I. INTRODUCTION

WILDFIRES, recognized as one of the most severe natural disasters globally, have exhibited a significant increase in intensity and frequency in recent years, destroying communities and ecosystems [1], [2]. Taking Canada as an example, 6551 wildfires occurred in 2023, burning more than 40 million acres, the largest burned area in the country's history. Hundreds of these

Manuscript received 28 February 2024; revised 11 May 2024; accepted 16 May 2024. Date of publication 20 May 2024; date of current version 14 June 2024. This work was supported in part by the National Key Research and Development Program of China under Grant 2023YFC3006805, and in part by the National Natural Science Foundation of China under Grant 31971668. (Corresponding author: Change Zheng; Fengjun Zhao.)

The authors are with the School of Technology, Beijing Forestry University, Beijing 100083, China, also with the Key Laboratory of Forest Protection of National Forestry and Grassland Administration, Ecology and Nature Conservation Institute, Chinese Academy of Forestry, Beijing 100091, China, and also with the Heilongjiang Ecological Engineering Vocational College, Heilongjiang 150025, China (e-mail: zhengchange@bjfu.edu.cn; zhaofj@caf.ac.cn).

Digital Object Identifier 10.1109/JSTARS.2024.3403146

wildfires spread over more than four months, resulting in the release of large amounts of greenhouse gases and air pollution from the fires that affected the atmosphere across Canada and even reached Europe. The accumulation of greenhouse gases in the atmosphere leads to global warming, which in turn triggers more extreme weather conditions such as abnormal rainfall, vegetation drying, strong winds, high temperatures, and high-frequency lightning strikes [3]. These conditions make vegetation more prone to ignition. Once ignited, the burning vegetation releases more greenhouse gases, exacerbating their accumulation in the atmosphere and further driving global warming. These processes create a reinforcing feedback loop, intensifying the frequency and intensity of wildfires [4].

While various methods are used to reduce the risk of wildfire, wildfires still occur due to lightning strikes and human carelessness, especially in extreme weather conditions [4]. The ability to accurately predict the spread of wildfires is crucial for effective wildfire management, including the timely deployment of firefighting resources, resident evacuation plans, and emergency response measures [5], [6].

Current wildfire spread prediction models focus on either the spread rate at each point on the fire line or the position of the fire line or burning area at the subsequent time step, representing the overall propagation and extent of the wildfire.

Fire-point spread rate predictions can be further subcategorized into two broad categories. First, empirical models establish relationships of fire spread rate based on experimental data [7], rendering them suitable for specific conditions but potentially inadequate in complex environments [8], [9]. Second, physical models [10], grounded in thermodynamic principles, analyze wildfire spread through the mechanisms of heat conduction, convection, and radiation, offering broader applicability. However, these two methods focus on the spread rate of one certain fire point and cannot predict large-scale fires, such as those using remote sensing as a data source. [11], [12].

Various mathematical models have been developed to predict not only the rate of spread but also to forecast the trend and shape of fire behavior. These models, utilizing mathematical equations and incorporating physical principles, construct detailed simulations of wildfire behavior. Ranging from the earliest Huygens' principle model [13] such as FARSITE [14] and graph

theory models [15], [16] to level set [17] and cellular automata (CA) [18], they have deepened the understanding of forest fire behavior by offering a 2-D perspective from local details to overall form, thus providing more comprehensive predictions of the path and shape of fire spread. Although, Huygens' principle and CA are commonly used as benchmark comparisons for newer models [16], [19]. The prediction principles of these models mostly require some prior knowledge and empirical formulas, which leads to questionable accuracy and insufficient scale to predict large-scale fires [20], [21].

The development of satellite and sensor technologies has facilitated the application of machine learning, specifically deep learning, in remote sensing. For instance, Hong et al. [22] constructed a novel collection of multimodal remote sensing benchmark datasets, encompassing hyperspectral, multispectral, and SAR data, to facilitate research on cross-city semantic segmentation tasks. Additionally, he proposed a high-resolution domain adaptation network to address the challenges associated with such tasks. Hong et al. [23] introduced SpectralGPT, a groundbreaking universal RS foundation model, specifically engineered to tackle spectral RS images using an innovative 3-D generative pretrained transformer (GPT). Li et al. [24] presented a new hyperspectral anomaly detection baseline network and demonstrated the model's scalability by displaying the good evaluation results of eight datasets.

Indeed, alongside the aforementioned general deep learning networks, there have been notable advancements in developing architectures tailored specifically for wildfire applications [25], [26]. For example, Fantine Huot [27] used Google Earth Engine (GEE) [28] to establish the "Next Day Wildfire Spread" dataset, incorporating MOD14A1 wildfire information (Fire mask band) and 11 remote sensing variables, and applied a convolutional autoencoder (AE) to predict the wildfire spread. The results have better accuracy than logistic regression and random forest models, thus, highlighting the potential for predicting wildfire spread using remote sensing imagery. Marjani et al. [29] established a dataset of wildfires across Canada and Alaska from 2001–2019, incorporating MCD14ML wildfire and environmental variables. The predicting model's architecture is divided into four parts: hourly, daily, constant, and combination modules to extract features from different modalities and perform binary prediction for each pixel. Comparative experiments were conducted on diverse combinations of loss functions, padding sizes, batch sizes, and thresholds, with the best model achieving over 90% accuracy. The study also analyzed the impact of environmental variables on fire behavior within the models.

All the methods mentioned above primarily focus on predicting either the spread rate of points on the fire line or the area of fire combustion. However, even with the recent integration of deep learning techniques into spreading prediction, the focus has mainly revolved around classifying individual pixels as either fire or nonfire, without providing insight into the burning intensity of the fire pixels [19], [30], [31]. Predicting the extent of fire spread alone cannot provide sufficient information to guide firefighting efforts. Lack of prediction of fire intensity may lead to uneven resource allocation and waste of limited firefighting resources. If we can accurately predict the intensity

of fire combustion and combine it with the area of fire spread, we can develop more reasonable resource allocation strategies to concentrate limited resources in the areas where the fire is most intense, in order to maximize the outcome of firefighting [32]. For example, we can prioritize aerial firefighting efforts in areas with higher fire intensity to maximize the impact of limited resources [33], [34], [35]. In addition, by predicting the intensity of fire combustion, we can better assess the degree of threat that fires pose to the environment and lives. For wildfires, understanding the burning intensity of each location can help us predict smoke diffusion, harmful gas emissions, and the impact of fires on surrounding vegetation and wildlife. These pieces of information are crucial for developing response measures, protecting the ecological environment, and ensuring life safety [36]. Therefore, the focus of our research is to address this gap by developing a novel approach that aims to predict the fire intensity at all locations within the area at the next timestep or several timesteps. This innovation has the potential to significantly enhance resource allocation and response strategies, ultimately improving the effectiveness and efficiency of firefighting efforts.

Fire intensity represents the energy released per unit area by the combustion of organic matter technically speaking, typically measured in Wm^{-2} , can broadly encompass fire line intensity, temperature, residence time, and radiative energy [37]. With advancements in remote sensing technology, we now have access to more extensive wildfire characteristic data [38]. Currently, remote sensing data related to wildfires are mainly divided into two categories: the burned area product [39] and the active fire product [38]. FRP, as an important part of active fire product, is commonly retrieved using the Wooster method, which involves calculating FRP at each identified fire pixel using midinfrared (MIR) radiometry. FRP not only reflects the thermal energy release of flames directly but also correlates significantly with biomass consumption [40], smoke emissions [36], aerosol optical depth (AOD) [34], [41], and particulate matter (PM) concentration [35]. In summary, accurately predicting FRP during wildfire spread is crucial for understanding fire behavior and its associated environmental pollution, making it an important parameter in fire behavior studies.

Despite the integration of mature FRP remote sensing products into various sensors, both geostationary (e.g., Meteosat Spinning Enhanced Visible and InfraRed Imager (SEVIRI) [42], Geostationary Operational Environmental Satellite (GOES) Advanced Baseline Imager (ABI) [43]) and polar-orbiting sensors (e.g., Aqua/Terra Moderate Resolution Imaging Spectroradiometer (MODIS) [44], Suomi National Polar-orbiting Partnership (Suomi NPP) Visible Infrared Imaging Radiometer Suite (VIIRS) [45]) have their limitations in accurately characterizing FRP. Geostationary sensors offer frequent retrieval but are limited by coarse spatial resolution, affecting the detection of subpixel fires and fires with low intensity. For instance, SEVIRI provides data every 15 min at a 3 km spatial resolution, hindering the detection of fires with FRP less than 50 MW [42], [46]. In contrast, polar-orbiting sensors can detect smaller and cooler fires but are limited by orbital characteristics, leading to lower temporal resolution. For example, VIIRS provides FRP products at 375 and 750 m resolutions only once

a day [45]. Therefore, fusion of data from both types of sensors can result in FRP images with high spatiotemporal resolution. So far, a fusion of sensors such as Himawari-8 and VIIRS [47], [48], along with MODIS and GOES [49], has shown promising results in subsequent fire emission assessments.

At present, there is a lack of relevant research and typical algorithms for real-time prediction of fire radiation power based on traditional methods or deep learning. We believe there are two main reasons for this. First, at the data level, the number and comprehensiveness of field samples are insufficient. Second, traditional methods make it difficult to handle multimodal data and predict nonlinear problems. In response to these two issues, a large amount of remote sensing data provides a dataset guarantee, and deep learning also has the ability to handle feature extraction and nonlinear modeling of grid-based images. Therefore, the main purpose of this study is to explore the potential of deep learning architectures in predicting fire radiation power in the field of remote sensing, rather than comparing them with traditional models.

To our knowledge, we are the first study to conduct FRP prediction of grid-based images. Based on this starting point, our approach is to model the FRP of remote sensing images using deep learning. There are three challenges in this work.

- 1) The accuracy of data affects the accuracy of the trained model, but FRP data have strong uncertainty [50] and the comprehensiveness of the impact factors on the wildfire dataset is lacking [27].
- 2) At present, there are many studies on deep learning in spatiotemporal modeling, but for complex multisource input problems such as wildfires, benchmark models have not yet been established [29].
- 3) In terms of deep learning modeling, model optimization, analysis of influencing factors, and temporal characteristics are important but difficult and insufficient [27].

We have completed the following tasks in response to the above challenges.

- 1) We combined MODIS and GOES FRP products to derive the fire diurnal cycle reasonably and collected remote sensing images of wildfire spread driving factors combined with corrected daily maximum FRP images to establish a dataset.
- 2) We developed a deep learning model framework specifically designed for analyzing remotely sensed multimodal data.
- 3) We performed optimization techniques to determine the optimal time series length and loss function given three different encoders¹ and discussed the impact of various driving factors on model prediction and the model's ability in transfer learning and multistep prediction.

The rest of this article is organized as follows. Section II introduces the sources and integration of data for historical remote-sensing data. Section III describes our network framework and evaluation metrics. Section IV optimized the time series length and loss function and demonstrated the model

prediction accuracy. Section V discusses the importance of input features and timeliness of the model, and finally, Section VI concludes this article.

II. DATASET

Using the data sources available in GEE [28], we propose a data aggregation workflow that combines historical fire events with remote sensing data.

A. Research Area and Motivation

The research area is chosen in California, United States, for two main reasons. First, approximately 33 million acres of forest in California encompass a wide variety of vegetation types and provide rich data and ecological diversity for research, as shown in Fig. 1(a) which illustrates 17 different land cover types. Second, due to the high frequency of fires, Fig. 1(b), illustrates the number of fires exceeding 10000 acres from 2017 to 2022, along with the total burned area. Our dataset contains significant fire incidents in California exceeding 10000 acres since 2017, totaling 88 cases. The fire data are sourced from the California Department of Forestry and Fire Protection (CALFIRE²). This offers a wealth of cases and a diverse ecological background for our research.

The data is collected at the precise locations and times of each fire incident within a 64-km by 64-km rectangular area. In this study, FRP is the core state object, also referred to as “state data,” while variables closely related to the spread of fire are considered as driving conditions, termed “condition data.” Condition data are further divided into two categories: one is “dynamic data,” primarily consisting of meteorological information, and the other is “constant data,” including static variables such as topography, vegetation, and human data. These have been widely recognized and implemented as driving factors for wildfire spread, and are used for purposes such as wildfire monitoring, prediction, and analysis [51], [52], [53]. Condition data can be also obtained through remote sensing. See Sections II-B and II-C for more information on remote sensing data sources, specific resolutions, and processing methods of each band.

B. State Data

As the predictive output for fire spread, our FRP data are a combination of MOD14A1, MYD14A1, and GOES-16Hot Spot Characterization(HSC). The MOD14A1 and MYD14A1 products are from the MODIS sensors on the Aqua and Terra satellites [44], respectively. The MaxFRP band data provided on GEE are updated once a day with a spatial resolution of 1 km. MaxFRP data represent the maximum fire radiative power (FRP) in each pixel, with the corresponding overpass times for the two products being approximately 1:30 P.M. and 10:30 A.M. [50]. However, the FRP at these moments may not capture the maximum value for the day, thus we apply an approach that integrates FRP products with high temporal resolution:

¹The data source, model code, and detailed training methodology are available at https://github.com/dazhaxie666/FRP_Prediction.

²[Online]. Available: <https://www.fire.ca.gov/>.

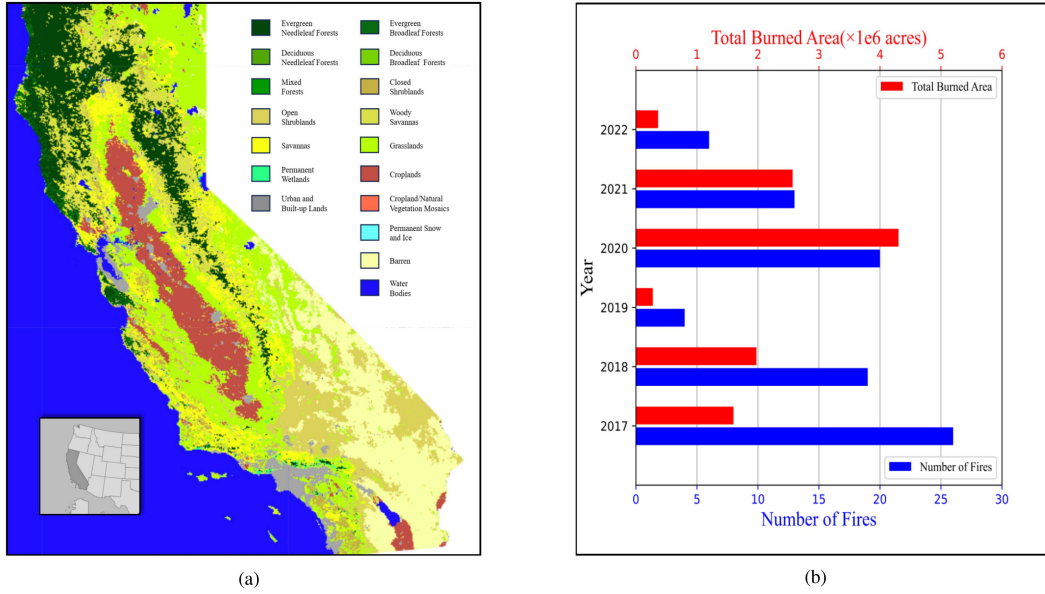


Fig. 1. (a) California land cover. (b) California fire incident statistics over the years.

first, determine the intensity distribution in time and then optimize it in the spatial domain. To achieve this, we select the GOES-16 HSC satellite, which provides FRP band data with a temporal resolution of 5 min and a spatial resolution of 4 km. Our approach is founded on the theories and outcomes of Andela et al. [54] and Zhang et al. [47], adapting and fine-tuning the aforementioned two types of sensor data. The first step is to utilize the high temporal resolution FRP data from GOES representing the fire intensity changes throughout the day for the entire area as a standard Gaussian distribution on an hourly basis [55]. The second step involves parameterizing the FRP for each pixel using the MaxFRP band data from both products and the established Gaussian function, with the GOES FRP as the baseline, to calculate the maximum FRP value. To obtain the MODIS-GOES FRP value at time t for a specific pixel j , refer to (1) shown at the bottom of this page. $FRP_{MODIS-GOES,j,t}$ is the instantaneous MODIS-GOES FRP(MW) for pixel j at time t ; $FRP_{night,j}$ is the night-time (01:00 LST) GOES FRP(MW) for pixel j ; $FRP_{Terra,j}$ is the daytime (10:30 LST) Terra FRP (MW) for pixel j ; $FRP_{Aqua,j}$ is the daytime (13:30 LST) Aqua FRP (MW) for pixel j ; t_{peak} and σ represent the mean and standard deviation of the GOES FRP diurnal cycle, which are calculated by fitting a Gaussian function using nonlinear least squares.

μ_1 and μ_2 are adjustment factors that are used to align the daytime overpass times of the Aqua and Terra satellites with the peak time of the fire diurnal cycle's weighted mean, which can be formulated as follows:

$$\mu_1 = e^{-\frac{(t_{Terra,j}-t_{peak})^2}{2\sigma^2}} \quad (2a)$$

$$\mu_2 = e^{-\frac{(t_{Aqua,j}-t_{peak})^2}{2\sigma^2}} \quad (2b)$$

where $t_{Terra,j}$ and $t_{Aqua,j}$ are the local times of the Terra and Aqua FRP observation for pixel j . In this work, to simplify data processing, we treat these two variables as constants, setting Terra's overpass at 10:30 and Aqua's at 13:30.

The value of pixel j is the maximum FRP for the day after substituting $t=t_{peak}$ in (1).

Fig. 2 presents three major fires occurring in 2018, 2020, and 2022, respectively: County Fire, Creek Fire, and McKinney Fire. The figure illustrates scatter plots of normalized FRP for every hour across three selected days within each of the three fires. Gaussian distribution fitting curves are utilized to depict the daily variation trends in fire intensity. It is evident that the fire intensity has a clear diurnal pattern, with very low intensity at night (the normalized value is almost 0) and peaking in the noon or afternoon, which is consistent with the conclusions of previous experiments [55], [56]. It is worth noting that the red dots within the MODIS gray stripes in the figure do not represent maximum values during the day. It suggests that the Max FRP values obtained from Aqua and Terra satellite observations may not represent the highest fire intensity within a day. Therefore, it is necessary to calibrate with data from the Geosynchronous Environmental Satellite (GOES) [43] to obtain more accurate fire intensity information.

C. Condition Data

1) *Dynamic Data*: The dynamic data in this article includes temperature, precipitation, wind speed, wind direction,

$$FRP_{MODIS-GOES,j,t} = FRP_{night,j} + \left(\frac{\mu_1(FRP_{Terra,j} - FRP_{night,j}) + \mu_2(FRP_{Aqua,j} - FRP_{night,j})}{2} \right) e^{-\frac{(t-t_{peak})^2}{2\sigma^2}}. \quad (1)$$

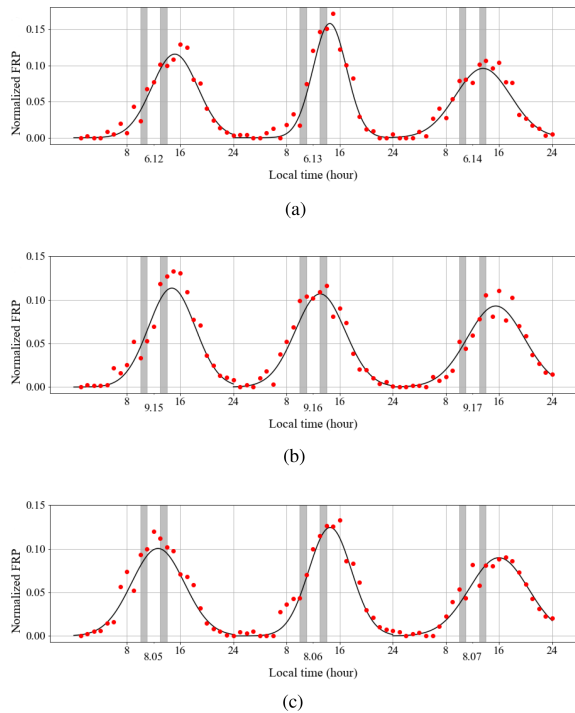


Fig. 2. (a) Time series of hourly normalized FRP derived from GOES data. Countyfire. For the first day, $t_{\text{peak}} = 15.2$ and $\sigma = 3.5$; for the second day, $t_{\text{peak}} = 12.5$ and $\sigma = 2.5$; for the third day, $t_{\text{peak}} = 13.6$ and $\sigma = 4.2$. (b) Creekfire. For the first day, $t_{\text{peak}} = 14.8$ and $\sigma = 3.5$; for the second day, $t_{\text{peak}} = 13.1$ and $\sigma = 3.7$; for the third day, $t_{\text{peak}} = 15.5$ and $\sigma = 4.3$. (c) McKinney Fire. For the first day, $t_{\text{peak}} = 12.7$ and $\sigma = 4.0$; for the second day, $t_{\text{peak}} = 14.6$ and $\sigma = 3.2$; for the third day, $t_{\text{peak}} = 16.0$ and $\sigma = 4.4$.

humidity, and dead combustible material moisture content. These data are sourced from the Gridded Surface Meteorological dataset (GRIDMET) [57], with a spatial resolution of 4 km for each band and a temporal resolution of 1 d, provided by the University of California, Merced.

2) *Constant Data*: The constant data include geographic, vegetation, and demographic data for the study area. Geographical data, such as elevation, aspect, and slope, are sourced from the Shuttle Radar Topography Mission (SRTM) [58] provided by NASA JPL at a resolution of 1 arc second. The landcover data are derived from the MODIS Version 6.1 Land Cover Type product (MCD12Q1) [59] on Terra and Aqua satellites. This product provides annual global land cover type data at a resolution of 500 m and is released and managed by the NASA Land Processes Distributed Active Archive Center (LP DAAC) under the U.S. Geological Survey (USGS) Earth Resources Observation and Science (EROS) Center. The vegetation remote sensing data are derived from the normalized difference vegetation index (NDVI) and enhanced vegetation index (EVI) band data of the VNP13A1 product on Suomi NPP VIIRS. Both bands provide important information about vegetation at a 500 m spatial resolution. NDVI is one of the most commonly used vegetation indices, typically employed to estimate the condition and health of surface vegetation. EVI [60], on the other hand, is an improved version of NDVI designed to overcome some of its limitations, particularly in cases of high and low vegetation cover. Population density data is obtained from the Gridded Population of World Version 4 (GPWv4) dataset by the Center for International Earth Science

Information Network (CIESIN) [61], with a resolution of 30 arc-seconds.

D. Data Aggregation and Preprocessing

All the above raw data can be obtained on GEE. To spatially align the data, we projected data from different sources onto the World Geodetic System 1984 (WGS1984) [27]. Considering the varying spatial resolutions of the data sources, we resampled all data to a consistent 1-kilometer resolution aligned with the state data using nearest-neighbor interpolation to reduce model complexity. Finally, normalization of the data using the min-max method was applied. Fig. 3 presents state data and dynamic data for one time step, along with the corresponding constant data for each fire incident. The higher the brightness of a pixel in the FRP image, the higher its FRP value. Before DL, we randomly split the data into training, validation, and test sets in a 7:1:2 ratio.

III. METHOD

A. Overview of the Framework

We developed a deep learning framework to predict fire radiant power utilizing multimodal data, as shown in Fig. 4. The prediction model proposed in this article belongs to the encoder-decoder framework. The encoder involves two components: the multimodal encoder and the backbone encoder. In the multimodal encoder, we established three blocks to process three types of data, to increase their number of channels without changing the height and width of the feature layers. The “State Block” and “Dynamic Block” spatiotemporal encoders, respectively, handle state data with a channel = 1 and dynamic data with a channel = 9. The spatiotemporal encoder, as the main part of the encoder, processes a large and complex amount of data and will choose from three modules with strong universality: 3-D CNN [62], I3-D [63], and ConvLSTM [64], [65], shown in Fig. 5. Although the Transformer model performs well in analogous fields, the three models are still feasible and effective choices for situations with relatively small sample sizes. They provide us with several flexible and reliable ways to process spatiotemporal data and have shown broad application prospects in spatiotemporal tasks similar to this article, such as radar echo prediction [66] and video prediction [65]. The spatial encoder in the “Constant Block” processes spatial data with a channel = 9 for constant data, where the architecture chosen is a typical CNN network [67]. Concatenate the outputs of three blocks and feed them into the Backbone Encoder as the final output of the Multimodal Encoder. The Backbone Encoder reduces the resolution of the feature map while increasing the channel depth, effectively compressing spatial information into a more abstract representation. The “Backbone Decoder” upsamples the bottleneck feature map, restoring it to a size consistent with the input dimensions. Both the Backbone encoder and decoder consist of stacked convolution (transposed convolution for the decoder) and pooling operations.

Additional details on model architecture are provided in Appendix A.

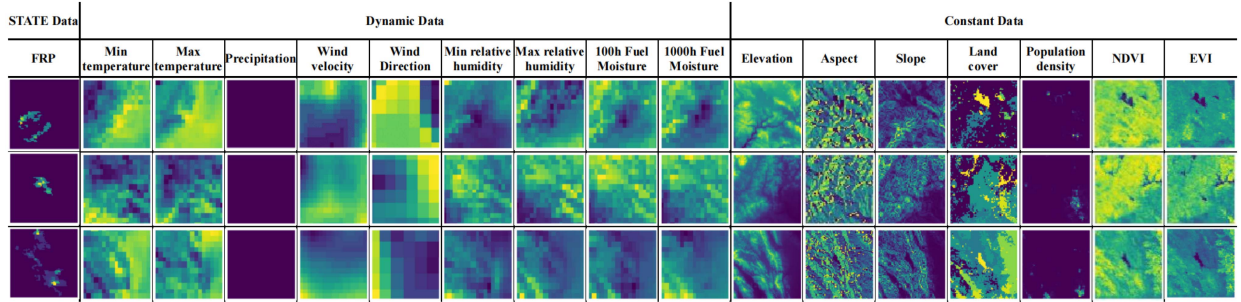


Fig. 3. Examples from our dataset. Each example is 64 km by 64 km, with a resolution of 1 km. In the examples, the fire incident in the first row is the Dixie Fire, which occurred on July 22, 2021; the fire incident in the second row is the Carr Fire, which occurred on July 26, 2018; and the fire incident in the third row is the LNU Lightning Complex, which occurred on August 19, 2020.

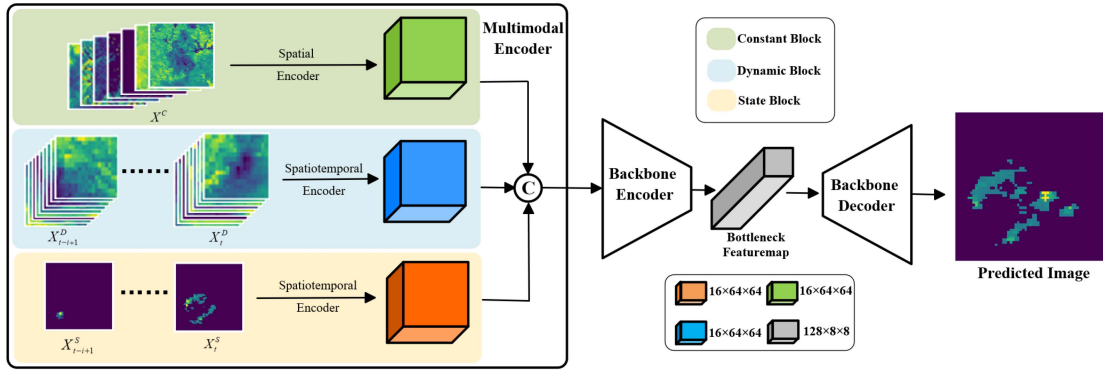


Fig. 4. Deep learning framework.

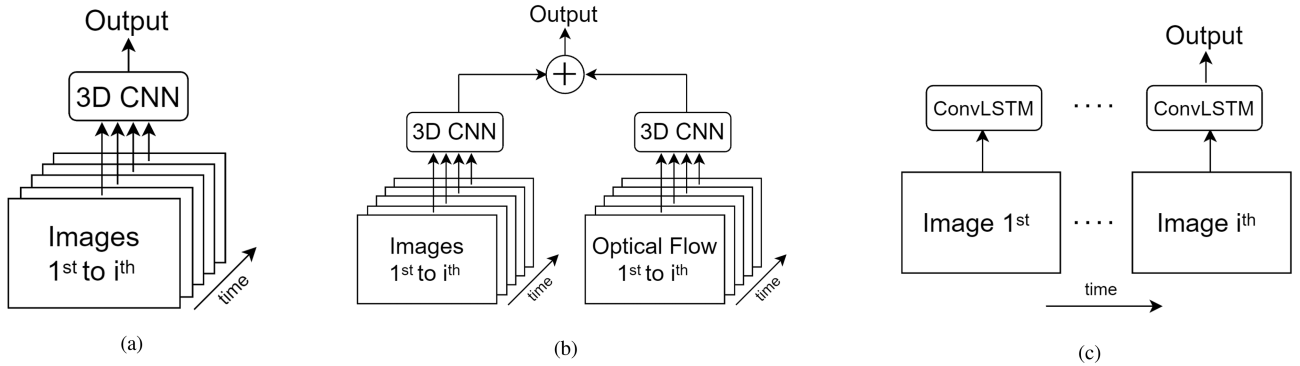


Fig. 5. (a) 3-D CNN. (b) I3-D. (c) ConvLSTM.

B. Evaluation Metrics

We use mean squared error (MSE) as our loss function, which is calculated as shown in the following:

$$L_{MSE} = \frac{1}{n} \sum_{i=1}^n (y_i - \hat{y}_i)^2 \quad (3)$$

where y_i represents the true value of the i th pixel, and \hat{y}_i represents the predicted pixel value at the same pixel location.

In this article, peak signal-to-noise ratio (PSNR) and structural similarity index (SSIM) are used as metrics [68]. PSNR measures the quality and distortion of an image by comparing the maximum pixel values and mean squared error between

the ground truth and the predicted image. SSIM is an index that measures the visual similarity of two images, taking into account elements such as luminance, contrast, and structure to evaluate image quality in a manner closer to human visual perception. Both are widely used in spatiotemporal and video prediction [69], with calculations detailed in the following:

$$PSNR = 10 \cdot \log_{10} \left(\frac{\text{MAX}_I^2}{\text{MSE}} \right) \quad (4)$$

$$SSIM(Y, \hat{Y}) = \frac{1}{M} \sum_{i=1}^M \left[\frac{(2\mu_{y_i} \mu_{\hat{y}_i} + c_1)(2\sigma_{y_i \hat{y}_i} + c_2)}{(\mu_{y_i}^2 + \mu_{\hat{y}_i}^2 + c_1)(\sigma_{y_i}^2 + \sigma_{\hat{y}_i}^2 + c_2)} \right] \quad (5)$$

where MAX_I is the maximum possible pixel value, in this article $\text{MAX}_I = 1$, MSE is the mean squared error between two grayscale images; M is the total number of windows within the image. y_i is the i th window of the original image Y , and \hat{y}_i is the corresponding i th window of the comparison (predicted) image \hat{Y} . μ_{y_i} and $\mu_{\hat{y}_i}$ are the average pixel value of the image window y_i and \hat{y}_i . $\sigma_{y_i}^2$ and $\sigma_{\hat{y}_i}^2$ are the variance of the image window y_i and \hat{y}_i . c_1 and c_2 are small constants to avoid division by zero. The value of PSNR ranges from 0 to infinity, and that of SSIM lies between 0 and 1; for both metrics, a larger value indicates greater similarity between the two images.

IV. EXPERIMENTS AND RESULTS

A. Training Details

To increase the diversity of the training dataset, reduce model overfitting, and enhance model robustness, we applied data augmentation in two spatial dimensions by using random cropping, random flipping, and random rotation. The model is trained using PyTorch. The training and testing phases are performed on a device equipped with an NVIDIA GeForce GTX 4070Ti GPU. The training consists of 1000 epochs with a learning rate of 0.0005, and the adaptive moment estimation (Adam) optimizer is used.

B. Performance With Varying Input Sequence Length

The impact of the input sequence length on deep learning models is complex [70]. Long sequences provide rich historical information, allowing the model to learn and identify more subtle and long-term trends, especially in scenarios where patterns and trends significantly change over time. However, processing long sequences may introduce irrelevant noise and increase the model's dependence on past data, thereby affecting its adaptability to new situations. At the same time, shorter sequences can significantly improve the model's computational efficiency and reduce delays caused by complex computations, which is particularly crucial for real-time prediction systems requiring fast responses. Balancing sequence length to maintain model performance while improving efficiency is an important aspect of designing spatiotemporal sequence prediction models. In this study, we conducted comparative experiments with sequence lengths ranging from 2 to 8 days to assess the impact of sequence length on model performance and efficiency, under the circumstance of three different spatiotemporal encoders (3-D CNN, I3-D, ConvLSTM). The results are shown in Table I.

The statistic in the table indicates that as the sequence length increases, the model's predictive performance significantly improves, which means that longer input sequences enhance the model's ability to capture the dynamics of forest fire propagation. However, as the sequence length becomes too long (with different values for different encoders), the performance indicators slightly decrease, and this change in performance trend may reflect the temporal dependence of wildfire behavior, where recent state and condition data have a greater impact on the spread of fires. The fire events in the dataset may mainly manifest as short-term behavioral patterns rather than cyclical

TABLE I
PERFORMANCE WITH VARYING SEQUENCE LENGTH

Sequence Length	3-D CNN		I3-D		ConvLSTM	
	PSNR	SSIM	PSNR	SSIM	PSNR	SSIM
2	18.2	52.2	18.2	53.2	17.5	51.2
3	20.6	59.1	20.9	60.8	19.0	56.6
4	23.2	63.9	22.5	62.9	21.5	62.9
5	22.2	62.7	22.4	62.9	23.3	64.9
6	22.9	63.2	23.1	64.2	25.3	68.9
7	22.6	63.1	22.9	63.6	25.2	68.7
8	22.5	63.1	22.6	63.3	25.1	68.2

The bold values represent the optimal model currently considering both SSIM and PSNR comprehensively.

or long-term trends [71]. In addition, during the training process, we found that longer sequence data can easily lead to overfitting. This situation occurs when the model excessively adapts to noise and less important feature details when attempting to capture complex patterns in training data [72]. Moreover, the optimal model under different spatiotemporal encoders corresponds to different optimal sequence lengths. Although 3-D CNN can process temporal information, it cannot explicitly handle long-term dependencies in time series. Therefore, in this dataset, recurrent neural networks can extract hidden layer information for each time step, resulting in higher accuracy [73].

Interestingly, it can be observed that there is not much difference in accuracy between 3-D CNN and I3-D, which is different from some previous studies [63]. We believe that this may be because, although both belong to the field of spatiotemporal sequence analysis, the temporal length of data in the field of wildfire spread is relatively short. The spatial resolution currently provided by satellites is insufficient compared to video prediction or video classification datasets, like sports motion and human action data. This missing information from the dataset makes it difficult for the model to extract the optical flow information during the wildfire spread period. In the dual stream network type I3-D, the optical flow branch module extracts a small amount of information. We extracted the weight ratio of the two branches in I3-D, with the spatiotemporal branch and the optical flow branch being 4.16:1. This validates our idea that the spatiotemporal branch extracts most of the wildfire spread features. For the subsequent experiments, we will select the models which were highlighted in bold for the following optimization.

C. Performance With Different Loss Function

For image output tasks, MSE is commonly used as the loss function to assess pixel-level errors. However, for the distinct structural characteristics of FRP during wildfire spread, simple MSE may overlook important structural features. Therefore, we propose a composite loss function that combines local MSE loss (L_{MSE}) for precision in detail and local SSIM loss (L_{SSIM}) for maintaining image structure integrity [74]. A series of experiments will be conducted to determine the optimal weighting between L_{MSE} and L_{SSIM} , aiming to enhance the model's performance in predicting wildfire FRP spread. The L_{SSIM} can be

TABLE II
PERFORMANCE WITH VARYING w_1 VALUES

w_1	3-D CNN		I3-D		ConvLSTM	
	PSNR	SSIM	PSNR	SSIM	PSNR	SSIM
1	23.7	63.9	23.6	64.2	25.3	68.9
0.9	23.7	64.2	24.1	64.7	25.6	69.0
0.8	23.5	64.9	23.9	67.5	25.5	73.1
0.7	23.6	66.8	23.7	68.9	25.0	73.2
0.6	21.0	64.9	23.8	69.1	24.8	73.9
0.5	18.9	59.2	23.9	68.2	24.8	73.7
0.4	17.2	56.4	20.8	64.3	24.4	69.2
0.3	16.9	56.6	20.1	62.7	20.6	65.1
0.2	15.1	51.7	17.7	58.9	13.7	54.9
0.1	12.0	42.3	13.9	57.3	11.3	51.3
0	10.8	31.6	11.3	57.6	9.9	42.6

The bold values represent the optimal model currently considering both SSIM and PSNR comprehensively.

calculated as follows:

$$L_{SSIM} = 1 - SSIM(Y, \hat{Y}) \quad (6)$$

where the calculation method for $SSIM(Y, \hat{Y})$ is presented in (5). The total loss can be calculated as follows:

$$L_{total} = w_1 L_{MSE} + w_2 L_{SSIM} \quad (7)$$

where w_1 is the weight coefficient for L_{MSE} , w_2 is the weight coefficient for L_{SSIM} , and it is defined that $w_2 = 1 - w_1$. The more similar the two images, the smaller L_{MSE} and L_{SSIM} become, resulting in a smaller L_{total} . We select the best-performing models, which have been highlighted in bold in Table I from the previous section, for the discussion on optimizing the loss function by increasing the weight of L_{SSIM} . The results are as shown in Table II.

The study results reveal that after integrating L_{SSIM} into the loss function, the predictive performance based on the PSNR and SSIM evaluation metrics initially improves slightly and then begins to decline. This indicates that an appropriate amount of L_{SSIM} can effectively enhance model training. Notably, PSNR and SSIM achieve the best predictive performance at different w_1 weight values, reflecting that these metrics assess image similarity from different aspects [75]. Relying entirely on L_{SSIM} for the loss function significantly decreases model performance in predicting fire-affected areas, likely due to the unique characteristics of the forest fire dataset, where fire areas are relatively sparse. SSIM scoring is based on structural similarity within image windows and averages the scores across windows, which may cause the model to overfit the nonfire windows during training, thereby neglecting key features of the fire areas such as contrast, brightness, and structure. We believe that in the realm of wildfire, the optimal model is verified by the task's demand for accurate predictions of spreading trends and precise identification of spreading areas, which are more crucial than simple pixel-level differences. Therefore, the model should focus more on the structural features of the images rather than merely on pixel value accuracy.

The visualization of partial prediction results from the currently best models, which are highlighted in bold in Table II, is shown in Fig. 6. The results indicate that the models exhibit a certain degree of imprecision in predicting details such as the

TABLE III
PERFORMANCE OF THE THREE MODELS

3-D CNN		I3-D		ConvLSTM	
PSNR	SSIM	PSNR	SSIM	PSNR	SSIM
22.9	59.0	22.8	59.1	23.3	60.9

periphery of the fire line, and it tends to merge scattered fire points into larger, merged fire sources or ignore small fires in the predicted image. This issue likely stems from inadequate information recovery during the upsampling phase of the network, which leads to the loss of nuanced edge and small fire spot details when transitioning from low to high-resolution data. The upsampling process is dependent on the model's ability to infer and augment details from learned patterns in the training data. A deficiency in the representation of these isolated fire patches within the training set, or a failure of the model's learning framework to sufficiently capture these features, may result in an inability to accurately reproduce small-scale fire patches, leading to the formation of larger, continuous fire zones. In terms of overall prediction performance, ConvLSTM outperforms both 3-D CNN and I3-D, as evident from both evaluation metrics and visualizations, particularly for regions with higher fire intensity.

The model exhibits acceptable consistency with real-world scenarios regarding the distribution of fire intensity and the morphology of fire spread. While the predictions may lack fine-grained details, the achieved level of precision still offers significant advantages for fire management and strategic deployment of firefighting resources.

V. DISCUSSION

A. Model Transferability

In the context of wildfire spread, model transferability denotes the capability of a model to effectively forecast wildfire activity in a different area or under varying conditions [29], [76]. To assess the transferability of our model trained by the dataset in California, we established an additional dataset comprising eight major fires in Alaska from May to August 2022 as a new test set. The format of the data is consistent with that of Section II and was input into the three optimized models described in Section IV, and the results are shown in Table III.

The predictive performance of these three models is similar in this additional dataset of Alaska. These results are lower than the predictive performance on the test set in California, and we attribute this to three main reasons. First, the geographical characteristics of Alaska differ significantly from those of California. For instance, most of Alaska's forested regions are located in boreal and temperate climate zones, whereas California is predominantly in a Mediterranean climate zone. The different climatic conditions lead to variations in vegetation types, growth cycles, and humidity levels, all of which directly affect the occurrence and spread of wildfires. Second, the difference in the seasonal patterns of wildfires between the two locations is also a crucial factor in the reduced model transferability. California's peak fire season typically occurs in the fall, in contrast to Alaska's late spring and early summer. Different


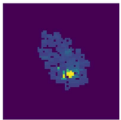
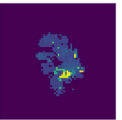
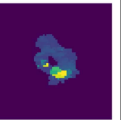
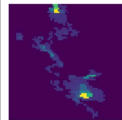
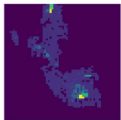
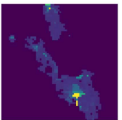
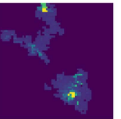
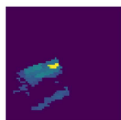


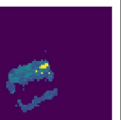
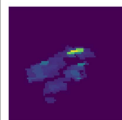
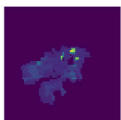


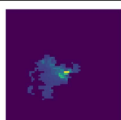
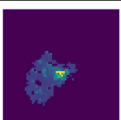
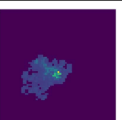
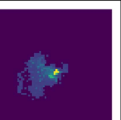
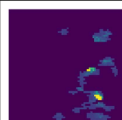
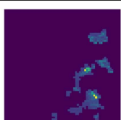


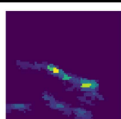
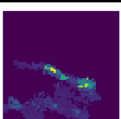
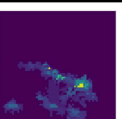
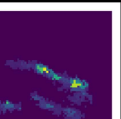
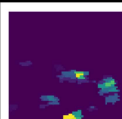
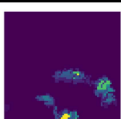
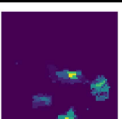
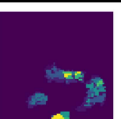
	Ground Truth	3D CNN	I3D	ConvLSTM	Ground Truth	3D CNN	I3D	ConvLSTM
								
PSNR(dB)		25.3	26.5	27.7		24.7	25.9	26.2
SSIM(%)		56.8	65.3	76.1		60.5	60.9	61.1
								
PSNR(dB)		26.3	27.1	28.1		25.3	24.7	27.1
SSIM(%)		62.1	70.3	75.2		63.5	63.6	65.9
								
PSNR(dB)		26.9	26.3	28.0		25.7	26.2	27.3
SSIM(%)		69.3	67.7	74.6		62.3	58.7	71.1
								
PSNR(dB)		25.3	24.4	28.7		26.8	25.2	27.1
SSIM(%)		59.2	58.3	77.7		64.3	62.6	63.5

Fig. 6. Eight sets of predicted images and ground truths, as well as the PSNR and SSIM between them. During visualization, if the predicted value on the predicted image is less than 100 MW, we set the value of that pixel to 0. There are two reasons for this. First, the FRP values in the input data, which indicate areas with fire, do not fall below 100 MW; second, adopting this threshold can effectively remove overly scattered points in the predicted image, thereby minimizing their impact on the visualization of the overall burned area.

seasonal patterns mean that the environmental conditions for wildfires, such as temperature, humidity, and wind speed, will also vary. Additionally, the impact of exceptional climatic events on wildfires cannot be overlooked. For example, the Hurricane Kay event in 2022 [77], [78] and the atmospheric river events in 2023 in California brought abnormal amounts of rainfall, which temporarily altered the regional drought conditions, thereby affecting the occurrence and spread of wildfires. Such sudden events are difficult to account for in model training, hence, they may lead to a decline in predictive performance in practical applications. We visualize the ground truth and predicted images for one day of each of the eight fires, along with their respective coordinates and predictive performance metrics, as shown in Fig. 7. In addition, the performance degradation of the transferred model in SSIM is slightly greater than that in PSNR, which may be due to the insufficient ability of the model to extract structural features from the new dataset. Despite a decline in performance evaluation metrics, the visualization results show that the model can still effectively predict the shape and intensity of wildfire spread. The models demonstrate basic predictive capabilities in new environments, proving their generality and adaptability. Therefore, the models are acceptable in terms of transferability and have practical value for wildfire prediction and management in varying areas.

B. Feature Sensitivity Analysis

To gain a better understanding of the importance of each channel in the model by using feature elimination [79], we conducted a channel ablation study. Specifically, we selected

various types of channels in the model and set their values to zero, then fed these altered inputs back into the trained optimal model to evaluate its performance [27]. In this process, the model will automatically learn which channels of information are more critical for the prediction task. By clearing specific channels and observing changes in model performance, we can infer that those channels that have a significant impact on performance contain important feature information required for prediction tasks [80]. The advantage of this method is that it can provide a quantitative evaluation of the relative importance of each channel in the model. By comparing the effects of each channel, we can identify the most critical channel for the task and further understand the model's behavior in feature extraction. If the model's performance significantly decreases after certain channels are zeroed out, it indicates that those channels have captured essential information for the prediction task. Table IV displays the feature types and the number of channels that were, along with the corresponding performance on the test set.

The model performance analysis shows that compared to using all features, removing the FRP state feature results in the most significant performance decline. This is because the distribution of FRP data is critical for the model to learn the FRP at the next moment, making the FRP state an indispensable input. For other types of features, the removal of anyone has a relatively small impact on model performance. However, the removal of topography and landcover data leads to a noticeable decrease in performance. This may be due to topography directly affecting the trend of fire spread, with the vegetation type and humidity conditions of different terrains affecting the spread of fire [81]. Additionally, landcover determines the type and distribution of

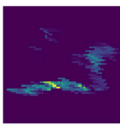
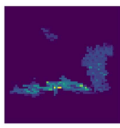
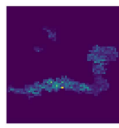
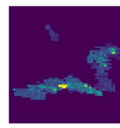
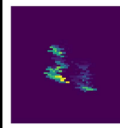
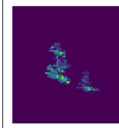
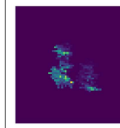
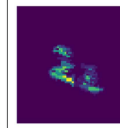
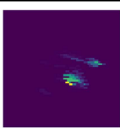
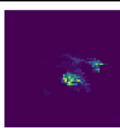
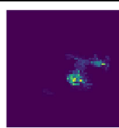
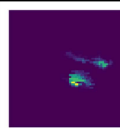
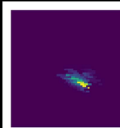
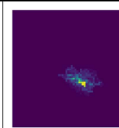
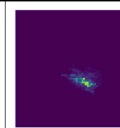
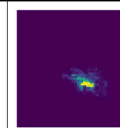
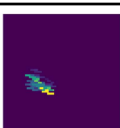
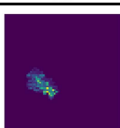
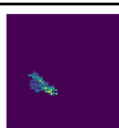
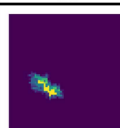
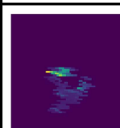
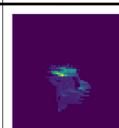
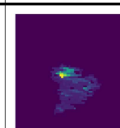
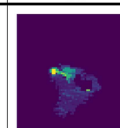
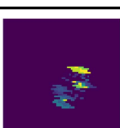

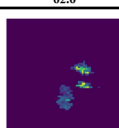

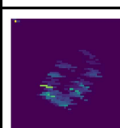
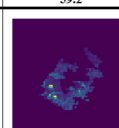
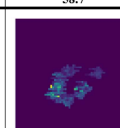
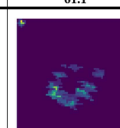
	Ground Truth	3D CNN	I3D	ConvLSTM	Ground Truth	3D CNN	I3D	ConvLSTM
								
PSNR(dB)		24.3	24.0	24.9		23.0	22.4	24.4
SSIM(%)		62.5	63.2	63.1		61.6	58.4	62.4
								
PSNR(dB)		23.5	23.3	25.3		23.7	22.7	24.3
SSIM(%)		60.3	60.9	63.5		63.5	58.9	59.8
								
PSNR(dB)		23.6	23.3	23.9		22.9	22.7	24.1
SSIM(%)		61.3	62.6	60.5		59.2	58.7	61.1
								
PSNR(dB)		22.5	22.6	24.3		23.8	23.2	24.7
SSIM(%)		56.3	58.3	60.1		60.3	58.6	62.9

Fig. 7. Eight sets of predicted images and ground truths in the additional dataset of Alaska, as well as the PSNR and SSIM between them.

TABLE IV
PERFORMANCE WITH REMOVED FEATURES

Removed Feature type	Number of Channel	3-D CNN		I3-D		ConvLSTM	
		PSNR (dB)	SSIM (%)	PSNR (dB)	SSIM (%)	PSNR (dB)	SSIM (%)
FRP State	1	4.3	23.7	5.6	25.4	7.6	34.6
Temperature	2	17.9	44.6	19.8	52.1	23.9	68.1
Precipitation	1	23.1	66.6	23.4	68.9	24.9	73.9
Wind	2	22.8	65.8	23.4	67.5	24.1	68.3
Humidity	1	23.3	66.9	23.9	68.1	24.7	72.4
Fuel Moisture	2	22.6	63.4	23.1	66.3	23.9	68.0
Topography	3	22.1	60.5	21.5	60.2	21.4	61.5
Landcover	1	22.1	59.2	22.1	62.9	22.4	64.2
Population density	1	23.4	65.0	23.7	67.3	25.0	74.0
Vegetation Index	2	23.3	64.5	23.4	67.5	24.3	71.5

combustible materials on the ground, which directly affects the intensity and speed of fire spread. The data in the table also show that removed features such as precipitation and population density do not decrease model accuracy, and may even increase it. The possible reason is that these two types of data are relatively sparse in the time and space domains; in the dataset of this article, precipitation data accounts for only 2.38% of the total number of days, while population density accounts for only 5.76% of the pixels in each image. These sparse data may be redundant for the model, and including these features could reduce the model's ability to extract important features. It is worth noting that, compared to the removal of constant information, the removal of dynamic information does not have a significant impact on the accuracy of the model. One possible reason is that the original spatial resolution of the dynamic information is relatively low, making it difficult to extract effective features. Another reason might be that the deep learning model has learned some dynamic meteorological information from the FRP state's time series data, whereas complex constant data is more difficult to learn.

In summary, through the discussion in this section, we can understand that removing some features will not significantly reduce the predictive performance of the model, which reduces the pressure of obtaining too much input data and the complexity of the model to cope with different research backgrounds (such as the unavailability of partial data from other regions).

C. Temporal Effectiveness of Multistep Prediction

While predicting the FRP value for the next day using data from the previous six days may provide a reference for fire departments, this information may not be sufficient for actual emergency fire response [82]. Therefore, this study further explores the effectiveness of the model in time series prediction, especially the transition from single-step to multistep forecasting. Considering that the results of Section V-B indicate that dynamic information contains more redundancy than static information and unknown dynamic information, we removed the dynamic information module and retrained the models to obtain the

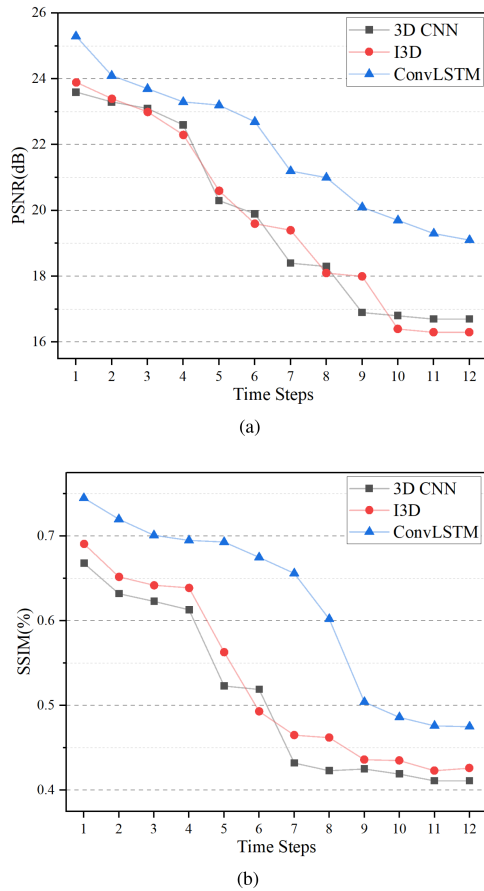


Fig. 8. (a) PSNR over increasing time steps. (b) SSIM over increasing time steps.

optimized version. Then, we iteratively predict using the model, taking the predicted FRP image data as new input to assess whether the models can maintain an acceptable level of accuracy in predicting the FRP values for the upcoming days based on the known FRP data and static information of the past six days [83]. The results are presented in Fig. 8(a) and (b).

The figure shows that, with input consisting only of state and constant data, all three models excel in single-step prediction, in line with the results of experiment Section V-B. In the multistep prediction, regardless of the type of spatiotemporal encoder, SSIMs remain above 61.7% and PSNR above 22.3 for the first four timesteps, indicating the model’s capacity for relatively accurate short-term FRP prediction. However, beyond four days, there is a marked decline in prediction accuracy, likely due to the gradual amplification of cumulative errors. In the process of multistep forecasting, errors from each step might propagate to the next, leading to an accumulation of errors in future predictions. As the number of time steps increases, the model’s ability to handle noisy and blurred input weakens, making it challenging to effectively restore image quality during upsampling, resulting in significant discrepancies in pixel-level detail as well as overall brightness, contrast, and structure compared to actual conditions. In summary, the model achieves acceptable accuracy for multistep forecasting up to four timesteps, with the capability to extend this step to six timesteps

using the ConvLSTM spatiotemporal encoder. This timeliness of the model is crucial in actual fire rescue operations, providing the fire department with rapid and accurate predictions of fire dynamics during the critical initial phase. Despite limitations in the length of prediction, the model remains a valuable tool for fire management and prevention.

VI. CONCLUSION

This article aims to extend deep learning to FRP prediction, a brand new research object for the spread of wildfires. To this end, we have utilized GEE to integrate the high temporal resolution FRP products from geostationary orbit satellites like GOES with those of high spatial resolution from polar orbit satellites, creating a new rasterized remote sensing imagery dataset with a daily temporal resolution where each pixel value represents the maximum value in that area. In conjunction with weather, topography, and vegetation characteristics, we created a multimodal dataset for the California region. To our knowledge, this is the first wildfire spread time series dataset containing FRP, which is essential for generating high-quality machine learning models for real-world fire scenarios.

To achieve reasonable predictions of FRP, we established a deep learning framework to handle this complex multimodal data. Given three different models, dynamic and constant data are encoded separately with different networks in the first layer, then merged and reencoded to generate a bottleneck feature map, and finally decoded back to the same data dimensions and size as our study subject, the FRP data.

We conducted research on input step size and optimized model prediction to ensure that our model maintains high accuracy while maintaining portability. Additionally, by incorporating L_{SSIM} into the overall loss function, experimental results indicate that the model performs well under dual assessment of SSIM and PSNR when L_{SSIM} is given a weight of 0.3 or 0.4. This result is consistent with the task of wildfire spread prediction because the model needs to understand the overall expansion pattern and structural shape of the spread to better assist people in grasping the patterns of fire behavior.

After obtaining the optimized model, to validate the model’s transferability, we tested it using wildfire data from Alaska in 2022. Although performance metrics indicate a decrease in predictive performance, visual results show that the model can still predict the overall shape and intensity distribution of the fires. Additionally, we conducted feature ablation experiments to delve deeper into the role of dynamic and static inputs in model performance. The experimental results revealed that static inputs contribute more significantly to the model than dynamic inputs in our dataset. By eliminating less important feature layers, the model can maintain accurate predictions. Moreover, this simplified approach also brings the added benefit of reducing the number of model parameters, thereby improving training efficiency. Ultimately, we analyzed the multistep prediction effects of the model using only static data and the FRP state processing module. The study found that within four timesteps, the model could maintain high predictive accuracy. However,

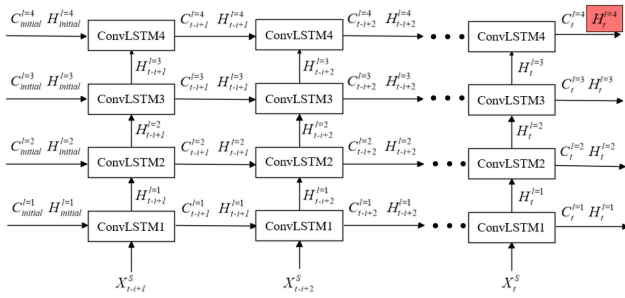
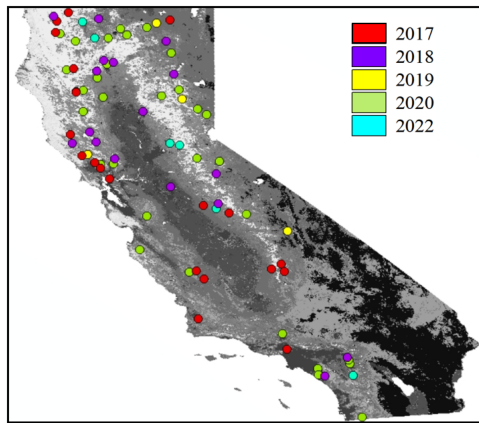
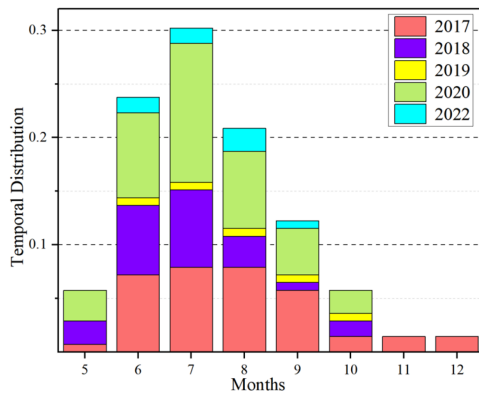


Fig. 10. Four layers ConvLSTM. The $H_{i+4}^{j=4}$ in the red box is the output from the ConvLSTM, used for subsequent convolution.



(a)



(b)

Fig. 11. (a) Spatial distribution. (b) Temporal distribution.

APPENDIX B SPATIOTEMPORAL DISTRIBUTION OF THE DATASET

Fig. 11 displays the spatial and temporal distribution of the dataset.

ACKNOWLEDGMENT

The authors would like to thank the Beijing Forestry University and the National Natural Science Foundation of China for their support, as well as all those who provided invaluable comments on this article. Additionally, the authors acknowledge the Beijing Super Cloud Center (BSCC) for providing HPC resources that have contributed to the research results reported in this paper.

REFERENCES

- [1] D. M. J. S. Bowman et al., "Fire in the earth system," *Science*, vol. 324, no. 5926, pp. 481–484, Apr. 2009, doi: [10.1126/science.1163886](https://doi.org/10.1126/science.1163886).
- [2] V. Iglesias, J. K. Balch, and W. R. Travis, "U.S. fires became larger, more frequent, and more widespread in the 2000s," *Sci. Adv.*, vol. 8, no. 11, Mar. 2022, Art. no. eabc0020, doi: [10.1126/sciadv.abc0020](https://doi.org/10.1126/sciadv.abc0020).
- [3] M. Goss et al., "Climate change is increasing the likelihood of extreme autumn wildfire conditions across California," *Environ. Res. Lett.*, vol. 15, no. 9, Aug. 2020, Art. no. 094016, doi: [10.1088/1748-9326/ab83a7](https://doi.org/10.1088/1748-9326/ab83a7).
- [4] A. Sullivan et al., "Spreading like wildfire: The rising threat of extraordinary landscape fires," 2022.
- [5] M. A. Finney, J. D. Cohen, S. S. McAllister, and W. M. Jolly, "On the need for a theory of wildland fire spread," *Int. J. Wildland Fire*, vol. 22, no. 1, 2013, Art. no. 25, doi: [10.1071/WF11117](https://doi.org/10.1071/WF11117).
- [6] W. G. Page, P. H. Freeborn, B. W. Butler, and W. M. Jolly, "A review of wildland firefighter entrapments: Trends, important environmental factors and research needs," *Int. J. Wildland Fire*, vol. 28, no. 8, 2019, Art. no. 551, doi: [10.1071/WF19022](https://doi.org/10.1071/WF19022).
- [7] A. L. Sullivan, "Wildland surface fire spread modelling, 1990–2007. 2: Empirical and quasi-empirical models," *Int. J. Wildland Fire*, vol. 18, no. 4, 2009, Art. no. 369, doi: [10.1071/WF06142](https://doi.org/10.1071/WF06142).
- [8] W. R. Anderson et al., "A generic, empirical-based model for predicting rate of fire spread in shrublands," *Int. J. Wildland Fire*, vol. 24, no. 4, 2015, Art. no. 443, doi: [10.1071/WF14130](https://doi.org/10.1071/WF14130).
- [9] M. G. Cruz, J. S. Gould, M. E. Alexander, A. L. Sullivan, W. L. McCaw, and S. Matthews, "Empirical-based models for predicting head-fire rate of spread in Australian fuel types," *Australian Forestry*, vol. 78, no. 3, pp. 118–158, Jul. 2015, doi: [10.1080/00049158.2015.1055063](https://doi.org/10.1080/00049158.2015.1055063).
- [10] A. L. Sullivan, "Wildland surface fire spread modelling, 1990–2007. 1: Physical and quasi-physical models," *Int. J. Wildland Fire*, vol. 18, no. 4, 2009, Art. no. 349, doi: [10.1071/WF06143](https://doi.org/10.1071/WF06143).
- [11] C. M. Hoffman et al., "Evaluating crown fire rate of spread predictions from physics-based models," *Fire Technol.*, vol. 52, no. 1, pp. 221–237, Jun. 2015, doi: [10.1007/s10694-015-0500-3](https://doi.org/10.1007/s10694-015-0500-3).
- [12] A. Simeoni, P. Salinesi, and F. Morandini, "Physical modelling of forest fire spreading through heterogeneous fuel beds," *Int. J. Wildland Fire*, vol. 20, no. 5, 2011, Art. no. 625, doi: [10.1071/WF09006](https://doi.org/10.1071/WF09006).
- [13] I. Knight and J. Coleman, "A fire perimeter expansion algorithm-based on Huygens wavelet propagation," *Int. J. Wildland Fire*, vol. 3, no. 2, 1993, Art. no. 73, doi: [10.1071/WF9930073](https://doi.org/10.1071/WF9930073).
- [14] M. A. Finney, "FARSITE, Fire area simulator—model development and evaluation," U.S. Department of Agriculture, Forest Service, Rocky Mountain Research Station, 4, 1998.
- [15] A. Stepanov and J. M. Smith, "Modeling wildfire propagation with Delaunay triangulation and shortest path algorithms," *Eur. J. Oper. Res.*, vol. 218, no. 3, pp. 775–788, May 2012, doi: [10.1016/j.ejor.2011.11.031](https://doi.org/10.1016/j.ejor.2011.11.031).
- [16] W. Jiang et al., "Modeling wildfire spread with an irregular graph network," *Fire*, vol. 5, no. 6, Nov. 2022, Art. no. 185, doi: [10.3390/fire5060185](https://doi.org/10.3390/fire5060185).
- [17] V. Mallet, D. Keyes, and F. Fendell, "Modeling wildland fire propagation with level set methods," *Comput. Math. Appl.*, vol. 57, no. 7, pp. 1089–1101, Apr. 2009, doi: [10.1016/j.camwa.2008.10.089](https://doi.org/10.1016/j.camwa.2008.10.089).
- [18] I. Karafyllidis and A. Thanailakis, "A model for predicting forest fire spreading using cellular automata," *Ecological Modelling*, vol. 99, no. 1, pp. 87–97, Jun. 1997, doi: [10.1016/S0304-3800\(96\)01942-4](https://doi.org/10.1016/S0304-3800(96)01942-4).
- [19] W. Jiang et al., "Wfnet: A hierarchical convolutional neural network for wildfire spread prediction," *Environ. Modelling Softw.*, vol. 170, Dec. 2023, Art. no. 105841, doi: [10.1016/j.envsoft.2023.105841](https://doi.org/10.1016/j.envsoft.2023.105841).
- [20] K. Zigner et al., "Evaluating the ability of farsite to simulate wildfires influenced by extreme, downslope winds in Santa Barbara, California," *Fire*, vol. 3, no. 3, Jul. 2020, Art. no. 29, doi: [10.3390/fire3030029](https://doi.org/10.3390/fire3030029).
- [21] X. Rui, S. Hui, X. Yu, G. Zhang, and B. Wu, "Forest fire spread simulation algorithm based on cellular automata," *Natural Hazards*, vol. 91, no. 1, pp. 309–319, Nov. 2017, doi: [10.1007/s11069-017-3127-5](https://doi.org/10.1007/s11069-017-3127-5).
- [22] D. Hong et al., "Cross-city matters: A multimodal remote sensing benchmark dataset for cross-city semantic segmentation using high-resolution domain adaptation networks," *Remote Sens. Environ.*, vol. 299, Dec. 2023, Art. no. 113856, doi: [10.1016/j.rse.2023.113856](https://doi.org/10.1016/j.rse.2023.113856).
- [23] D. Hong et al., "SpectralGPT: Spectral remote sensing foundation model," *IEEE Trans. Pattern Anal. Mach. Intell.*, 2024, to be published, doi: [10.1109/TPAMI.2024.3362475](https://doi.org/10.1109/TPAMI.2024.3362475).
- [24] C. Li, B. Zhang, D. Hong, J. Yao, and J. Chanussot, "LRR-Net: An interpretable deep unfolding network for hyperspectral anomaly detection," *IEEE Trans. Geosci. Remote Sens.*, vol. 61, 2023, Art. no. 5513412, doi: [10.1109/TGRS.2023.3279834](https://doi.org/10.1109/TGRS.2023.3279834).

- [25] L. Ma, Y. Liu, X. Zhang, Y. Ye, G. Yin, and B. A. Johnson, "Deep learning in remote sensing applications: A meta-analysis and review," *ISPRS J. Photogrammetry Remote Sens.*, vol. 152, pp. 166–177, Jun. 2019, doi: [10.1016/j.isprsjprs.2019.04.015](https://doi.org/10.1016/j.isprsjprs.2019.04.015).
- [26] G. H. de Almeida Pereira, A. M. Fusioka, B. T. Nassu, and R. Minetto, "Active fire detection in landsat-8 imagery: A large-scale dataset and a deep-learning study," *ISPRS J. Photogrammetry Remote Sens.*, vol. 178, pp. 171–186, Aug. 2021, doi: [10.1016/j.isprsjprs.2021.06.002](https://doi.org/10.1016/j.isprsjprs.2021.06.002).
- [27] F. Huot, R. L. Hu, N. Goyal, T. Sankar, M. Ihme, and Y.-F. Chen, "Next day wildfire spread: A machine learning dataset to predict wildfire spreading from remote-sensing data," *IEEE Trans. Geosci. Remote Sens.*, vol. 60, 2022, Art. no. 4412513, doi: [10.1109/TGRS.2022.3192974](https://doi.org/10.1109/TGRS.2022.3192974).
- [28] H. Tamiminia, B. Salehi, M. Mahdianpari, L. Quackenbush, S. Adeli, and B. Brisco, "Google Earth Engine for Geo-Big Data applications: A meta-analysis and systematic review," *ISPRS J. Photogrammetry Remote Sens.*, vol. 164, pp. 152–170, Jun. 2020, doi: [10.1016/j.isprsjprs.2020.04.001](https://doi.org/10.1016/j.isprsjprs.2020.04.001).
- [29] M. Marjani, S. A. Ahmadi, and M. Mahdianpari, "Firepred: A hybrid multi-temporal convolutional neural network model for wildfire spread prediction," *Ecological Informat.*, vol. 78, Dec. 2023, Art. no. 102282, doi: [10.1016/j.ecoinf.2023.102282](https://doi.org/10.1016/j.ecoinf.2023.102282).
- [30] F. Khennou and M. A. Akhloufi, "Improving wildland fire spread prediction using deep U-Nets," *Sci. Remote Sens.*, vol. 8, Dec. 2023, Art. no. 100101, doi: [10.1016/j.srs.2023.100101](https://doi.org/10.1016/j.srs.2023.100101).
- [31] D. Radočaj, M. Jurišić, and M. Gašparović, "A wildfire growth prediction and evaluation approach using landsat and modis data," *J. Environ. Manage.*, vol. 304, Feb. 2022, Art. no. 114351, doi: [10.1016/j.jenvman.2021.114351](https://doi.org/10.1016/j.jenvman.2021.114351).
- [32] M. A. Matos, A. M. A. C. Rocha, L. A. Costa, and F. Alvelos, "Resource dispatch optimization for firefighting based on genetic algorithm," in *Proc. Int. Conf. Comput. Sci. Appl.*, 2023, pp. 437–453. [Online]. Available: http://dx.doi.org/10.1007/978-3-031-37108-0_28
- [33] R. M. Clifford, S. Jung, S. Hoermann, M. Billingham, and R. W. Lindeman, "Creating a stressful decision making environment for aerial firefighter training in virtual reality," in *Proc. IEEE Conf. Virtual Reality 3D User Interfaces*, 2019, pp. 181–189, doi: [10.1109/VR.2019.8797889](https://doi.org/10.1109/VR.2019.8797889).
- [34] G. Pereira et al., "Estimating trace gas and aerosol emissions over south America: Relationship between fire radiative energy released and aerosol optical depth observations," *Atmospheric Environ.*, vol. 43, no. 40, pp. 6388–6397, Dec. 2009, doi: [10.1016/j.atmosenv.2009.09.013](https://doi.org/10.1016/j.atmosenv.2009.09.013).
- [35] J. W. Kaiser et al., "Biomass burning emissions estimated with a global fire assimilation system based on observed fire radiative power," *Biogeosciences*, vol. 9, no. 1, pp. 527–554, Jan. 2012, doi: [10.5194/bg-9-527-2012](https://doi.org/10.5194/bg-9-527-2012).
- [36] E. B. Wiggins et al., "High temporal resolution satellite observations of fire radiative power reveal link between fire behavior and aerosol and gas emissions," *Geophys. Res. Lett.*, vol. 47, no. 23, Dec. 2020, Art. no. e2020GL090707, doi: [10.1029/2020GL090707](https://doi.org/10.1029/2020GL090707).
- [37] J. E. Keeley, "Fire intensity, fire severity and burn severity: A brief review and suggested usage," *Int. J. Wildland Fire*, vol. 18, no. 1, 2009, Art. no. 116, doi: [10.1071/WF07049](https://doi.org/10.1071/WF07049).
- [38] M. J. Wooster et al., "Satellite remote sensing of active fires: History and current status, applications and future requirements," *Remote Sens. Environ.*, vol. 267, Dec. 2021, Art. no. 112694, doi: [10.1016/j.rse.2021.112694](https://doi.org/10.1016/j.rse.2021.112694).
- [39] E. Chuvieco et al., "Historical background and current developments for mapping burned area from satellite earth observation," *Remote Sens. Environ.*, vol. 225, pp. 45–64, May 2019, doi: [10.1016/j.rse.2019.02.013](https://doi.org/10.1016/j.rse.2019.02.013).
- [40] M. J. Wooster, G. Roberts, G. L. W. Perry, and Y. J. Kaufman, "Retrieval of biomass combustion rates and totals from fire radiative power observations: FRP derivation and calibration relationships between biomass consumption and fire radiative energy release," *J. Geophys. Res.: Atmos.*, vol. 110, no. D24, Dec. 2005, doi: [10.1029/2005JD006318](https://doi.org/10.1029/2005JD006318).
- [41] H. M. Nguyen and M. J. Wooster, "Advances in the estimation of high spatio-temporal resolution pan-African top-down biomass burning emissions made using geostationary fire radiative power (FRP) and maiaic aerosol optical depth (AOD) data," *Remote Sens. Environ.*, vol. 248, Oct. 2020, Art. no. 111971, doi: [10.1016/j.rse.2020.111971](https://doi.org/10.1016/j.rse.2020.111971).
- [42] M. J. Wooster et al., "Meteosat seviri fire radiative power (FRP) products from the land surface analysis satellite applications facility (LSA SAF) – Part 1: Algorithms, product contents and analysis," *Atmos. Chem. Phys. Discuss.*, vol. 15, no. 12, Jun. 2015, doi: [10.5194/acpd-15-15831-2015](https://doi.org/10.5194/acpd-15-15831-2015).
- [43] J. Hall, R. Zhang, W. Schroeder, C. Huang, and L. Giglio, "Validation of goes-16 ABI and MSG seviri active fire products," *Int. J. Appl. Earth Observ. Geoinf.*, vol. 83, Nov. 2019, Art. no. 101928, doi: [10.1016/j.jag.2019.101928](https://doi.org/10.1016/j.jag.2019.101928).
- [44] L. Giglio, W. Schroeder, and C. O. Justice, "The collection 6 modis active fire detection algorithm and fire products," *Remote Sens. Environ.*, vol. 178, pp. 31–41, Jun. 2016, doi: [10.1016/j.rse.2016.02.054](https://doi.org/10.1016/j.rse.2016.02.054).
- [45] I. Csiszar et al., "Active fires from the Suomi NPP visible infrared imaging radiometer suite: Product status and first evaluation results," *J. Geophys. Res.: Atmos.*, vol. 119, no. 2, pp. 803–816, Jan. 2014, doi: [10.1002/2013JD020453](https://doi.org/10.1002/2013JD020453).
- [46] G. J. Roberts and M. J. Wooster, "Fire detection and fire characterization over Africa using Meteosat SEVIRI," *IEEE Trans. Geosci. Remote Sens.*, vol. 46, no. 4, pp. 1200–1218, Apr. 2008, doi: [10.1109/TGRS.2008.915751](https://doi.org/10.1109/TGRS.2008.915751).
- [47] T. Zhang, M. C. de Jong, M. J. Wooster, W. Xu, and L. Wang, "Trends in eastern China agricultural fire emissions derived from a combination of geostationary (Himawari) and polar (VIIRS) orbiter fire radiative power products," *Atmospheric Chem. Phys.*, vol. 20, no. 17, pp. 10687–10705, Sep. 2020, doi: [10.5194/acp-20-10687-2020](https://doi.org/10.5194/acp-20-10687-2020).
- [48] Y. Zheng, J. Liu, H. Jian, X. Fan, and F. Yan, "Fire diurnal cycle derived from a combination of the Himawari-8 and VIIRS satellites to improve fire emission assessments in southeast Australia," *Remote Sens.*, vol. 13, no. 15, Jul. 2021, Art. no. 2852, doi: [10.3390/rs13152852](https://doi.org/10.3390/rs13152852).
- [49] F. Li, X. Zhang, D. P. Roy, and S. Kondragunta, "Estimation of biomass-burning emissions by fusing the fire radiative power retrievals from polar-orbiting and geostationary satellites across the conterminous United States," *Atmospheric Environ.*, vol. 211, pp. 274–287, Aug. 2019, doi: [10.1016/j.atmosenv.2019.05.017](https://doi.org/10.1016/j.atmosenv.2019.05.017).
- [50] P. H. Freeborn, M. J. Wooster, D. P. Roy, and M. A. Cochrane, "Quantification of modis fire radiative power (FRP) measurement uncertainty for use in satellite-based active fire characterization and biomass burning estimation," *Geophys. Res. Lett.*, vol. 41, no. 6, pp. 1988–1994, Mar. 2014, doi: [10.1002/2013GL059086](https://doi.org/10.1002/2013GL059086).
- [51] R. Ghali and M. A. Akhloufi, "Deep learning approaches for wildland fires using satellite remote sensing data: Detection, mapping, and prediction," *Fire*, vol. 6, no. 5, May 2023, Art. no. 192, doi: [10.3390/fire6050192](https://doi.org/10.3390/fire6050192).
- [52] J. K. Maingi and M. C. Henry, "Factors influencing wildfire occurrence and distribution in Eastern Kentucky, USA," *Int. J. Wildland Fire*, vol. 16, no. 1, 2007, Art. no. 23, doi: [10.1071/WF06007](https://doi.org/10.1071/WF06007).
- [53] M. Mhaweji, G. Faour, and J. Adjizian-Gerard, "Wildfire likelihood's elements: A literature review," *Challenges*, vol. 6, no. 2, pp. 282–293, Dec. 2015, doi: [10.3390/challe6020282](https://doi.org/10.3390/challe6020282).
- [54] N. Andela, J. W. Kaiser, G. R. van der Werf, and M. J. Wooster, "New fire diurnal cycle characterizations to improve fire radiative energy assessments made from modis observations," *Atmospheric Chem. Phys.*, vol. 15, no. 15, pp. 8831–8846, Aug. 2015, doi: [10.5194/acp-15-8831-2015](https://doi.org/10.5194/acp-15-8831-2015).
- [55] E. Ellicott, E. Vermote, L. Giglio, and G. Roberts, "Estimating biomass consumed from fire using modis FRE," *Geophys. Res. Lett.*, vol. 36, no. 13, Jul. 2009, doi: [10.1029/2009GL038581](https://doi.org/10.1029/2009GL038581).
- [56] X. Zhang, S. Kondragunta, J. Ram, C. Schmidt, and H. Huang, "Near-real-time global biomass burning emissions product from geostationary satellite constellation," *J. Geophys. Res.: Atmos.*, vol. 117, no. D14, Jul. 2012, doi: [10.1029/2012JD017459](https://doi.org/10.1029/2012JD017459).
- [57] J. T. Abatzoglou, "Development of gridded surface meteorological data for ecological applications and modelling," *Int. J. Climatol.*, vol. 33, no. 1, pp. 121–131, Dec. 2011, doi: [10.1002/joc.3413](https://doi.org/10.1002/joc.3413).
- [58] T. G. Farr et al., "The shuttle radar topography mission," *Rev. Geophys.*, vol. 45, no. 2, May 2007, doi: [10.1029/2005RG000183](https://doi.org/10.1029/2005RG000183).
- [59] D. Liang, Y. Zuo, L. Huang, J. Zhao, L. Teng, and F. Yang, "Evaluation of the consistency of modis land cover product (MCD12Q1) based on Chinese 30 m globeland30 datasets: A case study in Anhui Province, China," *ISPRS Int. J. Geo-Inf.*, vol. 4, no. 4, pp. 2519–2541, Nov. 2015, doi: [10.3390/ijgi4042519](https://doi.org/10.3390/ijgi4042519).
- [60] Z. Jiang, A. Huete, K. Didan, and T. Miura, "Development of a two-band enhanced vegetation index without a blue band," *Remote Sens. Environ.*, vol. 112, no. 10, pp. 3833–3845, Oct. 2008, doi: [10.1016/j.rse.2008.06.006](https://doi.org/10.1016/j.rse.2008.06.006).
- [61] E. Doxsey-Whitfield et al., "Taking advantage of the improved availability of census data: A first look at the gridded population of the world, version 4," *Papers Appl. Geogr.*, vol. 1, no. 3, pp. 226–234, Jul. 2015, doi: [10.1080/23754931.2015.1014272](https://doi.org/10.1080/23754931.2015.1014272).
- [62] D. Tran, L. Bourdev, R. Fergus, L. Torresani, and M. Paluri, "Learning spatiotemporal features with 3D convolutional networks," 2014. [Online]. Available: <https://arxiv.org/abs/1412.0767>
- [63] J. Carreira and A. Zisserman, "Quo vadis, action recognition? A new model and the kinetics dataset," 2017. [Online]. Available: <https://arxiv.org/abs/1705.07750>

- [64] S. Yao et al., "A ConvLSTM neural network model for spatiotemporal prediction of mining area surface deformation based on SBAS-InSAR monitoring data," *IEEE Trans. Geosci. Remote Sens.*, vol. 61, 2023, Art. no. 5201722, doi: [10.1109/TGRS.2023.3236510](https://doi.org/10.1109/TGRS.2023.3236510).
- [65] C. Shi, Z. Zhang, W. Zhang, C. Zhang, and Q. Xu, "Learning multiscale temporal-spatial-spectral features via a multipath convolutional LSTM neural network for change detection with hyperspectral images," *IEEE Trans. Geosci. Remote Sens.*, vol. 60, 2022, Art. no. 5529816, doi: [10.1109/TGRS.2022.3176642](https://doi.org/10.1109/TGRS.2022.3176642).
- [66] Y. Wang et al., "PredRNN: A recurrent neural network for spatiotemporal predictive learning," 2021. [Online]. Available: <https://arxiv.org/abs/2103.09504>
- [67] Z. Li, F. Liu, W. Yang, S. Peng, and J. Zhou, "A survey of convolutional neural networks: Analysis, applications, and prospects," *IEEE Trans. Neural Netw. Learn. Syst.*, vol. 33, no. 12, pp. 6999–7019, Dec. 2022, doi: [10.1109/TNNLS.2021.3084827](https://doi.org/10.1109/TNNLS.2021.3084827).
- [68] Y. Wang, L. Jiang, M.-H. Yang, L.-J. Li, M. Long, and L. Fei-Fei, "Eidetic 3D LSTM: A model for video prediction and beyond," in *Proc. Int. Conf. Learn. Representations*, 2018.
- [69] A. Hore and D. Ziou, "Image quality metrics: PSNR vs. SSIM," in *Proc. 20th Int. Conf. Pattern Recognit.*, 2010, pp. 2366–2369, doi: [10.1109/ICPR.2010.579](https://doi.org/10.1109/ICPR.2010.579).
- [70] Y. Yu, X. Si, C. Hu, and J. Zhang, "A review of recurrent neural networks: LSTM cells and network architectures," *Neural Comput.*, vol. 31, no. 7, pp. 1235–1270, Jul. 2019, doi: [10.1162/neco_a_01199](https://doi.org/10.1162/neco_a_01199).
- [71] A. Barbati, P. Corona, E. D'amato, and R. Cartisano, "Is landscape a driver of short-term wildfire recurrence?," *Landscape Res.*, vol. 40, no. 1, pp. 99–108, Apr. 2013, doi: [10.1080/01426397.2012.761681](https://doi.org/10.1080/01426397.2012.761681).
- [72] J. Zhao et al., "Do RNN and LSTM have long memory?," in *Proc. 37th Int. Conf. Mach. Learn.*, 2020, vol. 119, pp. 11365–11375. [Online]. Available: <https://proceedings.mlr.press/v119/zhao20c.html>
- [73] X. Shi, Z. Chen, H. Wang, D.-Y. Yeung, W.-K. Wong, and W.-C. Woo, "Convolutional LSTM network: A machine learning approach for precipitation nowcasting," in *Proc. Int. Conf. Adv. Neural Inf. Process. Syst.*, 2015, vol. 28, pp. 802–810.
- [74] H. Zhao, O. Gallo, I. Frosio, and J. Kautz, "Loss functions for image restoration with neural networks," *IEEE Trans. Comput. Imag.*, vol. 3, no. 1, pp. 47–57, Mar. 2017, doi: [10.1109/TCI.2016.2644865](https://doi.org/10.1109/TCI.2016.2644865).
- [75] U. Sara, M. Akter, and M. S. Uddin, "Image quality assessment through FSIM, SSIM, MSE and PSNR—A comparative study," *J. Comput. Commun.*, vol. 07, no. 3, pp. 8–18, 2019, doi: [10.4236/jcc.2019.73002](https://doi.org/10.4236/jcc.2019.73002).
- [76] C. Applestein, T. T. Caughlin, and M. J. Germino, "Weather affects post-fire recovery of sagebrush-steppe communities and model transferability among sites," *Ecosphere*, vol. 12, no. 4, Apr. 2021, Art. no. 3446, doi: [10.1002/ecs2.3446](https://doi.org/10.1002/ecs2.3446).
- [77] E. Blake, "The 2022 eastern Pacific hurricane season an above average season with five landfalls," *Weatherwise*, vol. 76, no. 4, pp. 27–35, Jun. 2023, doi: [10.1080/00431672.2023.2206755](https://doi.org/10.1080/00431672.2023.2206755).
- [78] J. Wang, M. J. DeFlorio, B. Guan, and C. M. Castellano, "Seasonality of MJO impacts on precipitation extremes over the western United States," *J. Hydrometeorol.*, vol. 24, no. 1, pp. 151–166, Jan. 2023, doi: [10.1175/JHM-D-22-0089.1](https://doi.org/10.1175/JHM-D-22-0089.1).
- [79] N. S. Escanilla, L. Hellerstein, R. Kleiman, Z. Kuang, J. Shull, and D. Page, "Recursive feature elimination by sensitivity testing," in *Proc. 17th IEEE Int. Conf. Mach. Learn. Appl.*, 2018, pp. 40–47, doi: [10.1109/ICMLA.2018.00014](https://doi.org/10.1109/ICMLA.2018.00014).
- [80] B. Choubin, A. Jaafari, J. Henareh, F. S. Hosseini, and A. Mosavi, "Averaged neural network integrated with recursive feature elimination for flood hazard assessment," in *Proc. IEEE 17th Int. Symp. Appl. Comput. Intell. Inform.*, 2023, pp. 000733–000738, doi: [10.1109/SACI58269.2023.10158640](https://doi.org/10.1109/SACI58269.2023.10158640).
- [81] M. Carmo, F. Moreira, P. Casimiro, and P. Vaz, "Land use and topography influences on wildfire occurrence in northern Portugal," *Landscape Urban Plan.*, vol. 100, no. 1/2, pp. 169–176, Mar. 2011, doi: [10.1016/j.landurbplan.2010.11.017](https://doi.org/10.1016/j.landurbplan.2010.11.017).
- [82] Y. Wang, M. Long, J. Wang, Z. Gao, and P. S. Yu, "PredRNN: Recurrent neural networks for predictive learning using spatiotemporal LSTMs," in *Proc. Int. Conf. Adv. Neural Inf. Process. Syst.*, 2017, vol. 30, pp. 879–888. [Online]. Available: https://proceedings.neurips.cc/paper_files/paper/2017/file/e5f6ad6ce374177ee0f23bf5d0c018b6-Paper.pdf
- [83] Y. Wang, Z. Gao, M. Long, J. Wang, and P. S. Yu, "PredRNN++: Towards a resolution of the deep-in-time dilemma in spatiotemporal predictive learning," in *Proc. 35th Int. Conf. Mach. Learn.*, 2018, vol. 80, pp. 5123–5132. [Online]. Available: <https://proceedings.mlr.press/v80/wang18b.html>



Zixun Dong received the B.E. degree in mechanical engineering in 2022 from Beijing Forestry University, Beijing, China, where he is currently working toward the M.S. degree in mechanical and electronic engineering.

His research interests include the pyrolysis of combustible biomass, wildfire monitoring, and spread prediction, and is dedicated to optimizing and exploring these fields through deep learning technology.



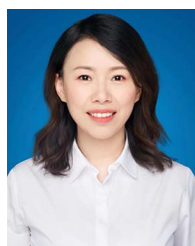
Change Zheng received the Ph.D. degree in robotics from the Beijing Institute of Technology, Beijing, China, in 2008.

She is currently a Professor with Beijing Forestry University, Beijing, China. Her research interests include forest fire and artificial intelligence.



Fengjun Zhao received the B.E. degree in forestry and the M.S. degree in botany from Beijing Forestry University, Beijing, China, in 1992 and 2004, respectively, and the Ph.D. degree in forest protection from the Chinese Academy of Forestry, Beijing, China, in 2007.

She is currently a Professor with the Ecology and Nature Conservation Institute, Chinese Academy of Forestry. Her research interests include forest fire prevention, forest fire mechanisms, fire behavior, fire spread model, fire monitoring and warning, fire ecology, etc.



Guangyu Wang received the master's degree in forestry engineering from Northeast Forestry University, Harbin, China, in 2009.

She is the Academic Leader with Forest Grassland Fire Prevention Technology Major, Heilongjiang Ecological Engineering Vocational College, Harbin, China. Her research interests include climate change and forest fires, forest fire risk assessment, and carbon emissions.

Ye Tian received the Ph.D. degree in mechanical design and theory from Beijing Forestry University, Beijing, China, in 2016.

He is currently an Associate Professor with Beijing Forestry University. His research interests include machine learning, computer vision, and plant phenotyping.



Hongchen Li received the B.E. degree in electrical engineering and automation from the School of Hebei University of Engineering, Hebei, China, in 2019, and the M.S. degree in electrical engineering from Lanzhou Jiaotong University, Lanzhou, China, in 2022. He is currently working toward the Ph.D. degree with Beijing Forestry University, Beijing, China.

His research interests include fire combustion, monitoring, spread prediction of wildfires based on deep learning, and remote sensing image recognition.